Plasmon-Enhanced Photocurrent from Photosystem I Assembled on Ag Nanopyramids

Ravi Pamu,[†,‖] V Prasad Sandireddy,[‡] Ramki Kalyanaraman,[‡,§] Bamin Khomami,*[,†,‡,⊥] and Dibyendu Mukherjee*[,†,‡,‖,⊥]

[†]Department of Mechanical, Aerospace, and Biomedical Engineering; [‡]Department of Chemical and Biomolecular Engineering; [§]Department of Material Science and Engineering; [‖]Nano-BioMaterials Laboratory for Energy, Energetics & Environment (nbml-E3); [⊥]Sustainable Energy Education and Research Center (SEERC), University of Tennessee, Knoxville, Tennessee 37996, United States

Ⓢ *Supporting Information*

ABSTRACT: Plasmonic metal nanostructures have been known to tune optoelectronic properties of fluorophores. Here, we report the first-ever experimental observation of plasmon-induced photocurrent enhancements from Photosystem I (PSI) immobilized on Fischer patterns of silver nanopyramids (Ag-NP). To this end, the plasmonic peaks of Ag-NP were tuned to match the PSI absorption peaks at ~450 and ~680 nm wavelengths. Specifically, the plasmon-enhanced photocurrents indicate enhancement factors of ~6.5 and ~5.8 as compared to PSI assembly on planar Ag substrates for nominal excitation wavelengths of 660 and 470 nm, respectively. The comparable enhancement factors from both 470 and 660 nm excitations, in spite of a significantly weaker plasmon absorption peak at ~450 nm for the Ag-NP structures, can be rationalized by previously reported excessive plasmon-induced fluorescence emission losses from PSI in the red region as compared to the blue region of the excitation wavelengths.
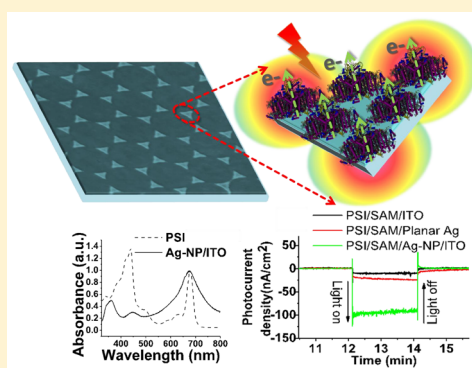
Natural photosynthetic processes harness solar energy with nearly 100% quantum efficiency. Central to this process is the supra-molecular protein Photosystem I (PSI) which acts as a biological photodiode and undergoes photochemical charge separation resulting in unidirectional electron transfer across the membrane-bound protein.[1,2] It is commonly proposed that the antennae chlorophylls and carotenoids in PSI channel the excitation energy to the reaction center chlorophyll pair (P700) via the Forster resonance energy-transfer mechanism[3] that initiates the electron transport pathway to the PSI acceptor terminals.[4−6] The robust structural and photoelectrochemical properties of cyanobacterial PSI[7] have inspired recent attempts in integrating it into solid-state bioelectronic devices,[8−11] biohybrid photovoltaic, solar H_2 production, and biosensor technologies.[6,12−19] To this end, a well-studied construct based on PSI immobilization on alkanethiolate hydrophilic self-assembled monolayer substrates that can allow optimal electron tunneling pathways has been developed.[20−25] More recent efforts have been directed to tune the photoresponse and photocurrent generation from PSI constructs confined in designer lipid bilayer membranes and conducting polymer scaffolds that mimic the natural thylakoid membrane housing of PSI.[26−29] However, the low light absorption capacities of these thin films prevents significant photocurrent generation from PSI monolayers.[19,30] A plausible strategy to circumvent such problems is to integrate PSI with plasmonic metal nanoparticles.[31] LSPR-induced collective

oscillations of surface electrons of the nanoparticles create highly localized electric fields and make absorption possible at resonant frequencies.

Localized surface plasmon resonance (LSPR) in noble metal nanostructures is known to modify emission and excitation rates in neighboring organic dyes and biomolecules[32] and enhance photocurrents in dye-sensitized[33−37] and organic solar cells.[38,39] Moreover, plasmon-enhanced photocurrents have been observed with other bacterial light-harvesting complexes.[40,41] However, the few studies conducted on plasmonic interactions of Au and Ag nanostructures with multichromophore-coupled PSI[31,42−48] have mostly focused on their unique effects on absorption and fluorescence emission characteristics. An interesting observation from these studies is the blue shift in the fluorescence emissions of PSI chromophores due to plasmonic interactions with red light excitation. Additionally, enhanced fluorescence in the 698−710 nm wavelength ranges of the PSI emission profile indicate fluorescence deactivation of higher-energy antenna chlorophylls. This should imply a reduction in energy-transfer efficiency between chlorophyll antennae and P700 responsible for charge separation and photocurrent generation. However, such high-energy emissions being virtually absent without plasmonic interactions might also

lead to activation of novel plasmon-induced pathways for chromophore−chromophore interactions and new energy-transfer pathways.[42,43,46] Such complex and intriguing photophysics of PSI coupled with plasmonic nanostructures underscores the critical yet unanswered questions regarding the alterations in photocurrent generations from plasmon-coupled PSI systems! Although the plasmon-enhanced photocurrents in PSI have not been measured, prior theoretical studies based on highly simplified photophysics of the process have suggested such enhancements.[48] Specifically, a prior study indicating enhanced photocurrents from PSI deposited on gold nanoparticle clusters has mostly ascribed the effect to the enhanced surface area from the nanoparticle clusters.[49] In fact, the aforementioned theoretical model for PSI coupled with Ag and Au spherical nanoparticles and nanoshells has revealed that, despite a reduced quantum yield, plasmon-induced electron production rates could undergo 6−15-fold enhancements for the various Ag and Au nanostructures at the resonant frequencies.[48]

This work not only provides experimental proof of LSPR-enhanced photocurrents from cyanobacterial PSI, assembled on plasmonic structures made out of Ag nanopyramids (Ag-NPs), but also confirms that relatively simple models of the photophysics of the system can indeed provide correct order of magnitude enhancement of the photocurrent.

The Ag-NPs with a dominant plasmon absorption peak at ~675 nm were fabricated by using a low-cost, facile, and high sample throughput nanosphere lithography (NSL) technique.[50] We discuss the results for the wavelength-dependent plasmon enhancement factors by comparing the photocurrent outputs from PSI assembled on plasmonic Ag-NPs and planar Ag for excitations at 395, 420, 470, and 660 nm wavelengths.

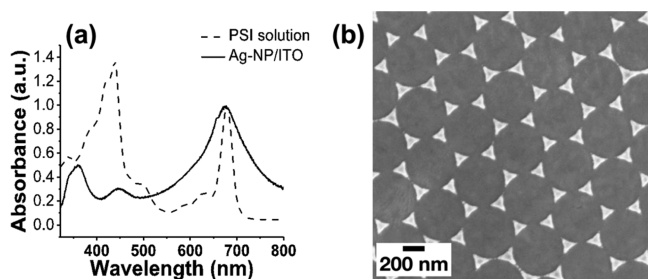Figure 1a shows the well-known absorbance peaks for colloidal suspensions of cyanobacterial PSI in aqueous

Figure 1. (a) Ultraviolet−visible absorbance spectra for PSI in solution and Ag nanopyramids (Ag-NPs) on ITO substrate. (b) SEM image showing Fischer patterned Ag-NP structures prepared via NSL technique.

solutions, i.e., 439 and 678 nm. The plasmonic resonance coupling with PSI requires the plasmon peaks of the fabricated metal nanostructures to overlap closely with the PSI absorption peaks.[48] To this end, the parameters of the NSL technique were tailored with optimized Ag deposition thickness and polystyrene beads diameter to result in the formation of the desired Ag-NP structures on the ITO wafer with overlapping absorbance at ~680 nm (see Figure 1). The plasmonic peak positions for the Ag NPs were found to be less sensitive to the thickness changes in the deposited Ag/Ag-NP heights but highly sensitive to the percentage of defects (bow tie-like structures) formed because of imperfect hexagonal packing of the polystyrene beads. It was observed that the Ag deposition

thickness of ~81 nm and polystyrene bead diameter of 500 nm results in the optimally designed Ag-NPs with the strongest broadband LSPR peak at ~675 nm that overlaps very closely with the PSI absorption peak at 678 nm (Figure 1). Additional lower-intensity absorption peaks centered at 447 and 360 nm are also observed for the Ag-NP plasmonic structures, as seen from Figure 1a. The 447 nm plasmonic absorption spreads over 410−485 nm; hence, it overlaps closely with the PSI broadband absorption peak at 439 nm in the violet-blue region. The as-fabricated Ag-NP structures are also visualized with scanning electron microscopy, as shown in Figure 1b depicting the regular Ag-NP triangular structures on ITO.

For direct comparison reported here for PSI on Ag-NP structures, control substrates of planar Ag on ITO with no plasmonic effects were also prepared. Planar Ag substrates are highly reflective with the transmission spectrum confirming the absence of any plasmonic peak absorptions. Additionally, bare flat ITO was selected as background electrode samples for comparison of measured photocurrents. As detailed in Experimental Methods, all three electrode samples of ITO, planar Ag, and Ag-NP/ITO, coated with SAM of OH-terminated C6 thiol, were incubated in PSI colloidal suspensions containing 0.02% w/v detergent to achieve PSI monolayer immobilization on the surfaces. The specific detergent concentration, resulting in 2.2 times the critical micellar concentration of DM surfactants (2.2CMC), has been shown to create PSI jammed colloidal suspensions that result in PSI monolayer formation during solution-phase incubation.[51] The PSI attachment to each of the three electrode samples was visualized with atomic force microscopy (AFM) before and after PSI/SAM coating.

As shown in Figure 2a, the homogeneous and smooth flat ITO substrate, with surface roughness <1 nm, starts indicating higher roughness and regular circular patches of densely packed PSI for the PSI/SAM coated ITO substrate shown in Figure 2b (the inset indicates approximate surface roughness ~6−7 nm and width of roughness profile ~25−30 nm). Similarly, the AFM image in Figure 2c for the planar Ag electrode surface
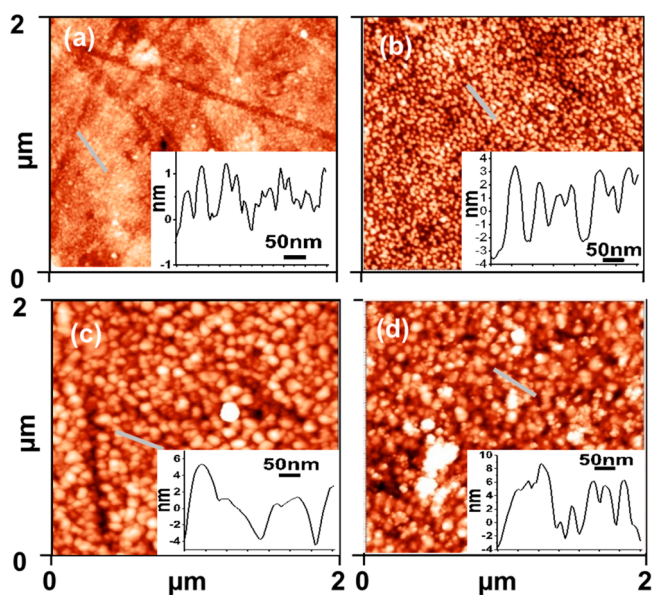

Figure 2. Topographical AFM images of flat ITO (a, b) and planar Ag/ITO (c, d) electrode substrates before (a, c) and after (b, d) PSI/thiol SAM assembly, respectively.

indicates polycrystalline Ag islands with roughness <10 nm and width ~60−100 nm. In contrast, the PSI assembled on planar Ag substrate in Figure 2d indicates sparse PSI distribution and cluster formations atop the Ag islands as also indicated by the inset showing line cross-sectional roughness of <7−8 nm and width of ~25- 30 nm on top of the wider cross-sectional profiles of Ag islands. The lack of visible dense PSI monolayer on this surface as compared to the ones on ITO could be attributed to the relatively higher surface roughness for the Ag island deposition. In conjunction, the AFM topographical images in Figure 3a,b for the Ag-NP/ITO substrates along with
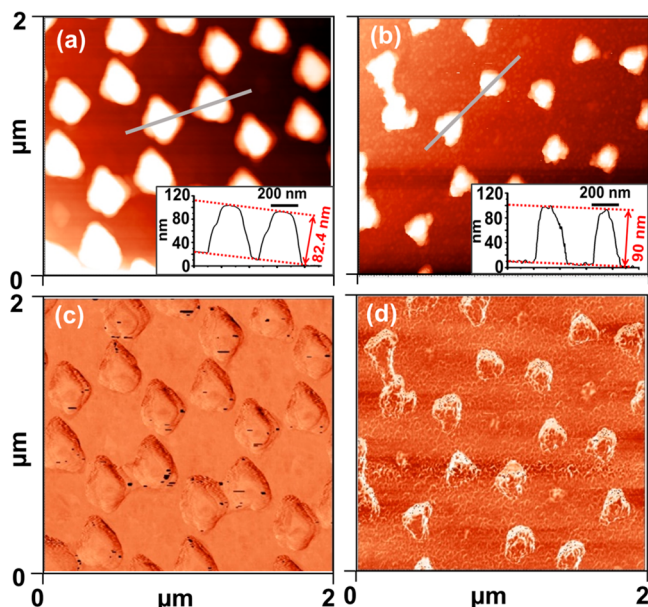

Figure 3. AFM images of Ag-NP/ITO substrates before (a) and after (b) PSI/SAM assembly along with the respective phase images for (c) Ag-NP/ITO and (d) PSI/SAM/Ag-NP/ITO substrates. (Insets: Height profiles across sections marked in panels a and b.)

respective phase images in Figures 3c,d clearly show the dense PSI monolayer formation on Ag-NPs and surrounding ITO areas. The cross-sectional height profiles of Ag-NPs with (~90 nm) and without (~82.4 nm) PSI coatings in Figure 3a,b insets also support this (typical PSI trimer height being ~9 nm). The uniform PSI attachments throughout the Ag-NP/ITO substrate is expected because the thiol SAM layer forms both on ITO and Ag surfaces during the incubation step in thiol solution. Finally, the diameter and height of the PSI complexes on all three electrode surfaces (in Figures 2b,d and 3d) are in agreement with our previous measurements of PSI monolayer on Au substrates.[30,51]

The wavelength-dependent plasmon-enhanced photocurrents from PSI was investigated using 4 LEDs with peak wavelengths at 395, 420, 470, and 660 nm as excitation light sources and 3 working electrodes of PSI assembled on SAM/X (X= flat ITO, planar Ag and Ag-NP/ITO) substrates. Specific photocurrent contributions from each of these substrates are deduced by subtracting the background photocurrents measured from the respective control SAM/X substrates. Figure 4a depicts a prototypical chronoamperometry (CA) data set for 660 nm light excitation indicating the stable photocurrents generated from the PSI/SAM/Ag-NP/ITO and the respective backgrounds from the control SAM/Ag-NP/ITO and Ag-NP/ITO substrates. To provide a clear comparison
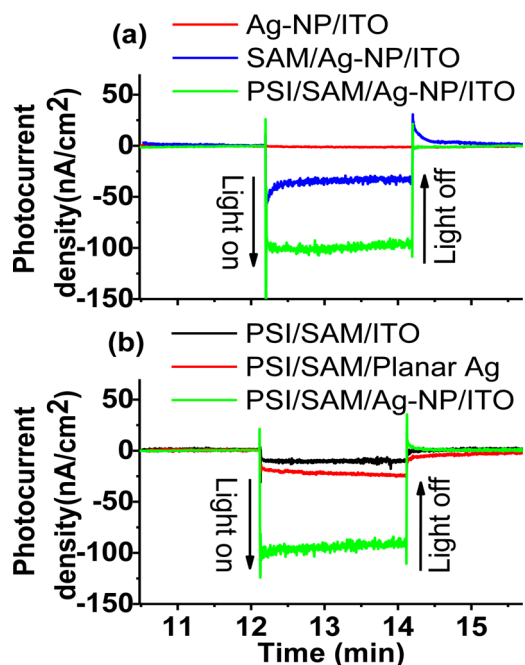

Figure 4. Chronoamperometry data of cathodic photocurrents (electron transfer from electrode through PSI to solution mediator) from light on−off experiments on (a) Ag-NP/ITO, SAM/Ag-NP/ITO, and PSI/SAM/Ag-NP/ITO substrates and (b) PSI/SAM/ITO, PSI/SAM/planar Ag, and PSI/SAM/Ag-NP/ITO at open-circuit potential under illumination from λ = 660 nm LED (36 mW/cm^2) in aqueous solution carrying 1 mM methyl viologen as charge carrier and 100 mM KCl as supporting electrolyte. (Ag/AgCl and Pt wire are used as reference electrode and counter electrode, respectively.)

with respect to photocurrents generated from PSI assembly on planar base substrates (devoid of Ag-NP structures) as the control working electrodes, Figure 4b also charts the CA data for PSI/SAM immobilized on flat ITO, and planar Ag along with the observed data for PSI/SAM/Ag-NP/ITO. It needs to be pointed out here that the working electrode with an effective 3.1 mm radius circular spot gets exposed to the charge carrier solution in the electrochemical cell. Hence, the nominal working area for the electrodes is 30.19 mm^2. For the results reported in Figure 4, this nominal area is taken as the effective working area for all the electrodes. In the case of planar Ag/ITO and flat ITO electrodes, the total exposed area is from the flat Ag surface and the ITO, respectively. In the case of the Ag-NP/ITO sample, the exposed area comprises a mixture of Ag areas in the form of Ag-NPs and the rest of the exposed ITO surfaces.

Figure 4 clearly demonstrate a distinct increase in the photocurrent generation during the light on period from the PSI/SAM/Ag-NP/ITO substrates as compared to the ones from either the SAM/Ag-NP/ITO (Figure 4a) or the PSI/SAM/planar Ag (Figure 4b) electrodes. These observations validate the specific photocurrent enhancements resulting from the presence of surface assembled PSI (Figure 4a) and more significantly, from the PSI assembly on the Fischer patterned SAM/Ag-NP/ITO substrates (Figure 4b). The minor photocurrent increases from SAM coating on both planar Ag and Ag NPs by itself (see Table S1 in the Supporting Information) can be attributed to work function changes of Ag surface due to the molecular dipole moments of attached thiol as also observed earlier.[52−57] Effective photocurrent contributions from surface

assembled PSI on each electrode X, as shown in Figure 5a, are subsequently estimated by subtracting the background photo-
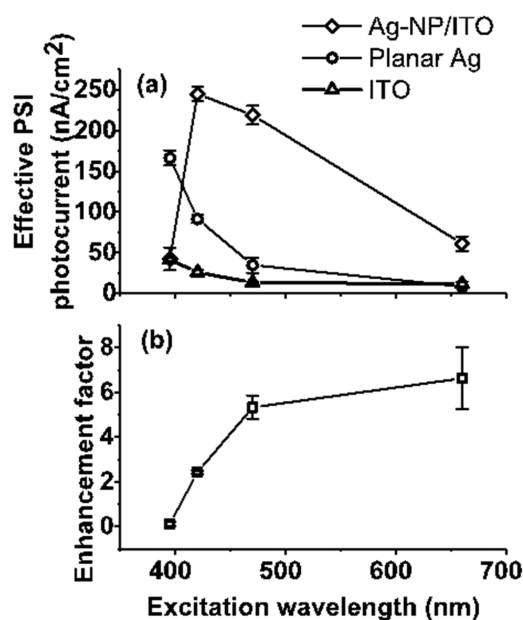

Figure 5. (a) Effective absolute value of photocurrents (PSI/SAM/X − SAM/X) from PSI assembly on electrodes where X = ITO, planar Ag, Ag-NP/ITO. (b) LSPR-induced photocurrent enhancement factors based on the ratio of effective photocurrents per PSI on Ag-NPs to that from planar Ag.

currents of SAM/X electrodes from the corresponding values of PSI/SAM/X electrodes (X = flat ITO, planar Ag, Ag-NP/ITO). Except for the PSI assembled on Ag-NP electrode, the effective PSI photocurrents show an increasing trend with decreasing wavelength of the light. This can be attributed to the nonplasmonic effects arising from enhanced photochemistry of surface adsorbed methyl viologen, and change of work function of the working electrode has also been commonly observed in earlier studies.[58] This effect is evidently predominant for the planar Ag as compared to the ITO electrodes.

It is also observed that the effective photocurrent for the PSI on the Ag-NP/ITO electrode is the lowest at 395 nm excitation and almost close to the value of the ITO electrode. In the absence of any plasmonic peak interactions with PSI at 375 nm (see Figure 1a), this observation can be simply explained by the relatively lower effects of the nonplasmonic initiated photocurrents largely from the PSI covered SAM/ITO surfaces because only 32% of the effective silver is in the form of Ag-NPs on the substrates (see the Supporting Information). The more interesting observation from Figure 5a is the trend in the effective photocurrents from PSI on Ag-NP/ITO electrode, when compared to that from PSI on planar Ag electrodes, clearly indicating a drastic increase at 420, 470, and 660 nm where the Ag-NP plasmonic peaks overlap with the dominant PSI absorption peaks. Such enhancements can be readily attributed to the localized plasmon-induced electric field enhancements from the Ag-NP structures coupling with the PSI systems to create pathways for enhanced absorption at the resonant frequencies.

Finally, the photocurrent enhancement factor from the LSPR-induced interactions of Ag-NPs with the PSI was calculated based on the photocurrent generation per PSI

trimer on each electrode which was deduced from the respective effective photocurrent densities and the PSI trimer number density on each electrode (see the Supporting Information for detailed calculation). Here, the increased additional surface area of 0.323 times the nominal surface area due to the 3D Ag nanostructures for the Ag-NP/ITO electrodes was accounted for in our calculations (Supporting Information). Because the PSI is uniformly distributed on both Ag-NPs and ITO parts of the Ag-NP/ITO electrode surfaces, the photocurrent recorded evidently has contributions from the PSI proteins immobilized on both the ITO and the Ag-NP areas. Here one needs to bear in mind that the electric field generated by LSPR is highly localized and typically undergoes rapid decay with distance from the plasmonic metal structures. Such observations have also been made in earlier studies indicating the rapid decay of evanescent field based on drastic decrease in the incident photon-to-current efficiency as distance between Ag nanoparticles and dye molecules in DSSC increased from 2 to 8 nm.[37] Because in the present study the thickness of PSI/SAM layers on Ag-NP surface is in the range of 8−10 nm, one can fairly assume that there will not be any plasmonic effect from the edges of the Ag-NP structures on PSI proteins attached to the ITO surface. Furthermore, because the photocurrent contribution from plain PSI/SAM/ITO electrode is minimal (Figure 5a), it is reasonable to assume that photocurrent contributions for the PSI/SAM/Ag-NP/ITO data could be decoupled between those from PSI on the ITO surface and PSI on Ag-NP surface to establish the actual plasmon-enhanced photocurrents.

To this end, the relative percentages of smooth ITO surface area and Ag-NP surface area are estimated from the SEM and AFM images of the Ag-NP/ITO surface (see the Supporting Information for detailed calculations of actual surface areas and PSI number densities on the various electrodes, and for the estimation of photocurrent densities per PSI as well as the enhancement factors). Hence, based on these deductions the photocurrent contributions per PSI attached to the Ag-NPs, the final plasmon-induced photocurrent enhancement factors are calculated as the ratio between the effective photocurrents per PSI on Ag-NP and planar Ag electrodes. The detailed geometric and mathematical calculations for the aforementioned estimations can be found in the Supporting Information. Based on these calculations, as seen from Figure 5b, the highest LSPR-induced photocurrent enhancement factor of ~6.5 is observed at the excitation wavelength of red light, $\lambda = 660$ nm. This can be clearly attributed to the strong coupling between the LSPR peak of the Ag-NP structures and the PSI absorption peak in the red region, i.e., $\lambda \sim 680$ nm in Figure 1a. It should be noted that the enhancement factors calculated here are conservative estimates because the presence of defects such as bow tie structures, presence of unremoved polystyrene beads, absence of Fischer pattern areas, etc. cannot be accurately accounted for. Such defects arise because of the defects in hexagonal packing of spherical beads and imperfect sonication.

The relatively lower enhancement factors of ~2.4 and ~5.8 at the 420 and 470 nm excitations, respectively, are due to the coupling between the broad Ag-NPs LSPR peak at 410−485 and the PSI absorption peak centered at ~450 nm. Also, the enhancement factor observed at 470 nm is higher than that at 420 nm because of the relatively higher plasmon resonance at 470 nm. However, the relatively weak increase (5.8 to 6.5) in the enhancement factors while going from 470 to 660 nm excitation is more counterintuitive because the plasmonic peak

at ~660 nm is more dominant than the peak at ~470 nm for the Ag-NPs. These discrepancies can be rationalized by the observations from past studies that under plasmonic interactions, PSI fluorescence emissions from 470 nm excitation indicate very low excitation energy loss as compared to the fluorescence energy loss pathways from 660 nm excitations.[42,43] Specifically, plasmon-induced fluorescence enhancement studies at room temperature shows a 200-fold fluorescence enhancement for 640 nm excitation as compared to a 17-fold enhancement with 485 nm excitation.[43] In fact, the distinct blue shift in the fluorescence signature of PSI coupled with plasmonic nanostructures undergoing red light excitation (640 and 680 nm) clearly indicates new excitation transfer pathways between chlorophylls.[42,43] Hence, the many-fold fluorescence enhancement from higher-energy chlorophylls which otherwise could have transferred that energy to P700 reaction center leads to significant reduction in the PSI charge separation efficiency.[42,43] Thus, photocurrent enhancement for PSI coupled to plasmonic nanostructures is expected to be less efficient with red light excitations. In accord with these observations, Figure 5b shows that the photocurrent enhancement factor has a relatively weaker increase for the 660 nm excitation than what was expected because of the presence of a stronger plasmonic peak at 675 nm, especially when compared to the enhancement factor for the 470 nm excitation.

To substantiate our hypothesis, regular Ag nanodot patterns (Ag-ND) were sputter coated on ITO substrates as controls with a broadband plasmonic absorption peak centered at around ~500 nm (Figures S2 and S3). Unlike the Fischer pattern studies presented earlier, here the plasmonic absorption at ~470 nm was higher than the corresponding absorption at ~660 nm for this control samples. Consequently, similar procedures as reported above for PSI immobilization, photocurrent testing, and enhancement factor calculations were followed. In this case, the effective enhancement factor under the nominal excitation wavelength of 470 nm was observed to be higher (almost twice) than the corresponding value with the 660 nm excitation, thereby qualitatively corroborating our earlier hypothesis that the fluorescent emission loss pathways for 470 nm excitation is weaker than the loss pathways for 660−680 nm excitation.

In conclusion, our work presents the first-ever experimental observation of photocurrent enhancements due to plasmon induced electric field in cyanobacterial PSI immobilized on Fischer patterns of Ag-NP structures. This was achieved by tuning the plasmonic absorption peak of Ag-NPs to the absorption peak of PSI at ~675−680 nm wavelengths. A large PSI photocurrent enhancement factor of ~6.5 was noted for λ = 660 nm excitation of PSI assembled on Ag-NP/ITO surfaces as compared to PSI on nonplasmonic planar Ag electrodes under similar conditions. The photocurrent enhancement factors increased only slightly from the excitations at 470 nm to the excitation at 660 nm owing to the enhanced plasmon-induced fluorescence emission losses for red light excitations as compared to blue light excitations. The fundamental findings of the current work are crucial in designing rational biotic−abiotic interfaces for future biohybrid solar energy-harvesting technologies.

■ EXPERIMENTAL METHODS

Sample Preparation. Commercial 50−80 nm thick ITO coated sodium lime glass substrates (NANOCS: IT100-111-25) cut into 1 cm × 1 cm size were first cleaned in RCA with 5:1:1 volume fractions of H_2O:30% NH_4OH:30% H_2O_2 with 15 min of sonication to remove the organic residues. The substrates were further sonicated in DI water for 15 min. All solvent and washing agents (NH_4OH, H_2O_2) were purchased from Fisher Chemicals. Planar Ag substrates were prepared by depositing Ag on cleaned ITO substrates in high vacuum (~1 × 10^{-8} Torr) by electron beam deposition (Model Mantis QUAD-EV-C) at room temperature. For Ag-NP preparations, 500 nm size polystyrene latex beads in a 2.5 wt % dispersion (Alfa Aesar-42714) were diluted with ethanol in 1:10 volume fractions first. The diluted beads solution was added drop by drop onto the base of the Petri dish glass partially filled (not covering the entire base) with DI water. Each drop pushed close to the Petri dish glass−water−air triple interface. The surface tension gradient forces the beads to migrate to the surface of water in the dish. This process is repeated until the beads cover the entire water surface with high packing density. The Petri dish was then carefully filled with water. The hexagonally packed monolayer of the beads with lowest defects was identified with its interference pattern on the water surface and scooped onto a clean ITO substrate. Following this procedure, 81 ± 4 nm thick Ag was deposited using an electron beam deposition method. Finally, the polymer bead mask was removed by sonication in ethanol for less than 1 min, leaving behind the Ag-NP Fischer patterns on ITO.

Each of the ITO, planar Ag, and Ag-NP/ITO substrates was thiolated by immersing it in 5 mM 6-mercapto-1-hexanol (obtained from Sigma-Aldrich) solution in ethanol for 7 days under N_2 environment and at room temperature. Subsequently, the as-obtained SAM/ITO, SAM/planar Ag, and SAM/Ag-NP/ITO substrates were thoroughly rinsed with isopropanol to remove any unbound thiol molecules. While sonication is a preferred method for ensuring only monolayer formation, such treatments were found to dislodge the Ag-NPs from the ITO surface and hence were not applied here. The PSI complexes from the wild-type PCC6803 were acquired from the stock solution that was prepared and reported in an earlier work.[59] For PSI immobilization, the SAM-coated wafers were immersed in 0.013 μM PSI solution with 0.02% w/v n-dodecyl-β-D-maltoside surfactant in aqueous 200 mM sodium phosphate buffer (pH 7) for 24 h in the dark at room temperature. The PSI/SAM/ITO, PSI/SAM/planar Ag, and PSI/SAM/Ag-NP/ITO substrates were finally thoroughly rinsed with DI water and dried under pressurized N_2.

Sample Imaging. A Zeiss Merlin SEM with accelerating voltage of 3 kV was used to image the Ag-NP/ITO electrode surface. Plasmonic resonance peak measurements were obtained via optical transmission spectrum of Ag-NP/ITO electrodes which were measured with an HR2000 + ES spectrometer from Ocean Optics. All surface topography images were collected on an NT-MDT AFM instrument in the tapping mode using silicon cantilever tips compatible with softer biological materials (NT-MDT; model NSG03). The tip had a force constant of 0.35−6.1 N/m along with a resonant frequency of 90 kHz.

Electrochemistry Measurements. All CA measurements were carried out with an electrochemistry setup using a potentiostat from Bio-Logic (model SP-300) and performed in a custom built standard three-electrode electrochemical cell where ITO, planar Ag, and Ag-NP/ITO substrates were used as the working electrodes; Pt wire as counter electrode; and Ag/AgCl (sat. NaCl) as the reference electrode (BAS Inc.; model MF-2052). A 1 mM sample of aqueous methyl viologen was used as

the soluble electron scavenger along with 100 mM KCl used as the supporting electrolyte. The four collimated LEDs purchased from ThorLabs with the nominal wavelengths of 395, 420, 470, and 660 nm (models M395L4, M420L3, M470L3, and M660L4) were operated with a power density of 36 mW/cm^2 reaching the working area when the solution in the cell was absent. The LED power densities were measured using a power meter purchased from ThorLabs (model S302C). All chronoamperometric measurements were performed at open-circuit voltage with the on−off light cycles being operated with 2 min intervals each and repeated for at least six cycles. The results reported are based on averaging the system response over six cycles.

■ ASSOCIATED CONTENT

Ⓢ Supporting Information

The Supporting Information is available free of charge on the ACS Publications website at DOI: 10.1021/acs.jpclett.7b03255.

> Photocurrent sample data and plasmon-induced photo-current enhancement factors calculations for PSI on Ag-NP and Ag-ND substrates (PDF)

■ AUTHOR INFORMATION

Corresponding Authors

*E-mail: dmukherj@utk.edu.
*E-mail: bkhomami@utk.edu.

ORCID Ⓘ

Dibyendu Mukherjee: 0000-0002-9232-6774

Author Contributions

R.P. designed and performed all the experiments. V.P.S. and R.K. contributed toward the fabrication of Ag-NP substrates via the NSL technique. D.M. and B.K. designed and supervised the overall research. All authors contributed to the data interpretation and analyses. All authors wrote and reviewed the manuscript.

Notes

The authors declare no competing financial interest.

■ ACKNOWLEDGMENTS

■ REFERENCES

(1) Nelson, N.; Yocum, C. F. Structure and Function of Photosystems I and II. *Annu. Rev. Plant Biol.* **2006**, *57*, 521−565.

(2) Nelson, N. Plant Photosystem I - The Most Efficient Nano-Photochemical Machine. *J. Nanosci. Nanotechnol.* **2009**, *9*, 1709−1713.

(3) Fromme, P.; Jordan, P.; Krauß, N. Structure of Photosystem I. *Biochim. Biophys. Acta, Bioenerg.* **2001**, *1507*, 5−31.

(4) Setif, P. Q.; Bottin, H. Laser Flash Absorption Spectroscopy Study of Ferredoxin Reduction by Photosystem I in Synechocystis sp. PCC 6803: Evidence for Submicrosecond and Microsecond Kinetics. *Biochemistry* **1994**, *33*, 8495−8504.

(5) Grotjohann, I.; Fromme, P. Structure of Cyanobacterial Photosystem I. *Photosynth. Res.* **2005**, *85*, 51−72.

(6) Lubner, C. E.; Grimme, R.; Bryant, D. A.; Golbeck, J. H. Wiring Photosystem I for Direct Solar Hydrogen Production. *Biochemistry* **2010**, *49*, 404−414.

(7) Jordan, P.; Fromme, P.; Witt, H. T.; Klukas, O.; Saenger, W.; Krauss, N. Three-Dimensional Structure of Cyanobacterial Photosystem I at 2.5 Angstrom Resolution. *Nature* **2001**, *411*, 909−917.

(8) Ko, B. S.; Babcock, B.; Jennings, G. K.; Tilden, S. G.; Peterson, R. R.; Cliffel, D.; Greenbaum, E. Effect of Surface Composition on the Adsorption of Photosystem I Onto Alkanethiolate Self-Assembled Monolayers on Gold. *Langmuir* **2004**, *20*, 4033−4038.

(9) Das, R.; Kiley, P. J.; Segal, M.; Norville, J.; Yu, A. A.; Wang, L. Y.; Trammell, S. A.; Reddick, L. E.; Kumar, R.; Stellacci, F.; et al. Integration of Photosynthetic Protein Molecular Complexes in Solid-State Electronic Devices. *Nano Lett.* **2004**, *4*, 1079−1083.

(10) Carmeli, I.; Frolov, L.; Carmeli, C.; Richter, S. Photovoltaic Activity of Photosystem I-Based Self-Assembled Monolayer. *J. Am. Chem. Soc.* **2007**, *129*, 12352−12353.

(11) Frolov, L.; Rosenwaks, Y.; Carmeli, C.; Carmeli, I. Fabrication of a Photoelectronic Device by Direct Chemical Binding of the Photosynthetic Reaction Center Protein to Metal Surfaces. *Adv. Mater.* **2005**, *17*, 2434−2437.

(12) Andrews, D. L. *Photonics, Biomedical Photonics, Spectroscopy, and Microscopy*; Wiley: Hoboken, NJ, 2015.

(13) Ciesielski, P. N.; Hijazi, F. M.; Scott, A. M.; Faulkner, C. J.; Beard, L.; Emmett, K.; Rosenthal, S. J.; Cliffel, D.; Jennings, G. K. Photosystem I−Based Biohybrid Photoelectrochemical Cells. *Bioresour. Technol.* **2010**, *101*, 3047−3053.

(14) LeBlanc, G.; Gizzie, E.; Yang, S.; Cliffel, D. E.; Jennings, G. K. Photosystem I Protein Films at Electrode Surfaces for Solar Energy Conversion. *Langmuir* **2014**, *30*, 10990−11001.

(15) Efrati, A.; Lu, C.-H.; Michaeli, D.; Nechushtai, R.; Alsaoub, S.; Schuhmann, W.; Willner, I. Assembly of Photo-Bioelectrochemical Cells Using Photosystem I-Functionalized Electrodes. *Nat. Energy* **2016**, *1*, 15021.

(16) Saboe, P. O.; Conte, E.; Chan, S.; Feroz, H.; Ferlez, B.; Farell, M.; Poyton, M. F.; Sines, I. T.; Yan, H.; Bazan, G. C.; et al. Biomimetic Wiring and Stabilization of Photosynthetic Membrane Proteins with Block Copolymer Interfaces. *J. Mater. Chem. A* **2016**, *4*, 15457−15463.

(17) Lubner, C. E.; Heinnickel, M.; Bryant, D. A.; Golbeck, J. H. Wiring Photosystem I for Electron Transfer to a Tethered Redox Dye. *Energy Environ. Sci.* **2011**, *4*, 2428−2434.

(18) Lubner, C. E.; Applegate, A. M.; Knorzer, P.; Ganago, A.; Bryant, D. A.; Happe, T.; Golbeck, J. H. Solar Hydrogen-Producing Bionanodevice Outperforms Natural Photosynthesis. *Proc. Natl. Acad. Sci. U. S. A.* **2011**, *108*, 20988−20991.

(19) Terasaki, N.; Yamamoto, N.; Tamada, K.; Hattori, M.; Hiraga, T.; Tohri, A.; Sato, I.; Iwai, M.; Iwai, M.; Taguchi, S.; et al. Bio-Photosensor: Cyanobacterial Photosystem I Coupled with Transistor via Molecular Wire. *Biochim. Biophys. Acta, Bioenerg.* **2007**, *1767*, 653−659.

(20) Carmeli, I.; Frolov, L.; Carmeli, C.; Richter, S. Photovoltaic Activity of Photosystem I-Based Self-Assembled Monolayer. *J. Am. Chem. Soc.* **2007**, *129*, 12352−12353.

(21) Mukherjee, D.; May, M.; Vaughn, M.; Bruce, B. D.; Khomami, B. Controlling the Morphology of Photosystem I Assembly on Thiol-Activated Au Substrates. *Langmuir* **2010**, *26*, 16048−16054.

(22) Mukherjee, D.; Vaughn, M.; Khomami, B.; Bruce, B. D. Modulation of Cyanobacterial Photosystem I Deposition Properties on Alkanethiolate Au Substrate by Various Experimental Conditions. *Colloids Surf., B* **2011**, *88*, 181−190.

(23) Lee, I.; Lee, J. W.; Greenbaum, E. Biomolecular Electronics: Vectorial Arrays of Photosynthetic Reaction Centers. *Phys. Rev. Lett.* **1997**, *79*, 3294.

(24) Ciesielski, P. N.; Scott, A. M.; Faulkner, C. J.; Berron, B. J.; Cliffel, D. E.; Jennings, G. K. Functionalized Nanoporous Gold Leaf Electrode Films for the Immobilization of Photosystem I. *ACS Nano* **2008**, *2*, 2465–2472.

(25) Ciobanu, M.; Kincaid, H. A.; Lo, V.; Dukes, A. D.; Jennings, G. K.; Cliffel, D. E. Electrochemistry and Photoelectrochemistry of Photosystem I Adsorbed on Hydroxyl-Terminated Monolayers. *J. Electroanal. Chem.* **2007**, *599*, 72–78.

(26) Saboe, P. O.; Conte, E.; Chan, S.; Feroz, H.; Ferlez, B.; Farell, M.; Poyton, M. F.; Sines, I. T.; Yan, H. J.; Bazan, G. C.; et al. Biomimetic Wiring and Stabilization of Photosynthetic Membrane Proteins with Block Copolymer Interfaces. *J. Mater. Chem. A* **2016**, *4*, 15457–15463.

(27) Saboe, P. O.; Lubner, C. E.; McCool, N. S.; Vargas-Barbosa, N. M.; Yan, H.; Chan, S.; Ferlez, B.; Bazan, G. C.; Golbeck, J. H.; Kumar, M. Two-Dimensional Protein Crystals for Solar Energy Conversion. *Adv. Mater.* **2014**, *26*, 7064–7069.

(28) Niroomand, H. S.; Mukherjee, D.; Khomami, B. Tuning the Photoexcitation Response of Cyanobacterial Photosystem I via Reconstitution into Proteoliposomes. *Sci. Rep.* **2017**, *7*, 2492.

(29) Niroomand, H.; Venkatesan, G. A.; Sarles, S. A.; Mukherjee, D.; Khomami, B. Lipid-Detergent Phase Transitions During Detergent-Mediated Liposome Solubilization. *J. Membr. Biol.* **2016**, *249*, 523–538.

(30) Bennett, T.; Niroomand, H.; Pamu, R.; Ivanov, I.; Mukherjee, D.; Khomami, B. Elucidating the Role of Methyl Viologen as a Scavenger of Photoactivated Electrons from Photosystem I Under Aerobic and Anaerobic Conditions. *Phys. Chem. Chem. Phys.* **2016**, *18*, 8512–8521.

(31) Carmeli, I.; Lieberman, I.; Kraversky, L.; Fan, Z.; Govorov, A. O.; Markovich, G.; Richter, S. Broad Band Enhancement of Light Absorption in Photosystem I by Metal Nanoparticle Antennas. *Nano Lett.* **2010**, *10*, 2069–2074.

(32) Dulkeith, E.; Morteani, A.; Niedereichholz, T.; Klar, T.; Feldmann, J.; Levi, S.; Van Veggel, F.; Reinhoudt, D.; Möller, M.; Gittins, D. Fluorescence Quenching of Dye Molecules Near Gold Nanoparticles: Radiative and Nonradiative Effects. *Phys. Rev. Lett.* **2002**, *89*, 203002.

(33) Akiyama, T.; Nakada, M.; Terasaki, N.; Yamada, S. Photocurrent Enhancement in a Porphyrin-Gold Nanoparticle Nanostructure Assisted by Localized Plasmon Excitation. *Chem. Commun.* **2006**, 395–7.

(34) Jeong, N. C.; Prasittichai, C.; Hupp, J. T. Photocurrent Enhancement by Surface Plasmon Resonance of Silver Nanoparticles in Highly Porous Dye-Sensitized Solar Cells. *Langmuir* **2011**, *27*, 14609–14.

(35) Lin, S.-J.; Lee, K.-C.; Wu, J.-L.; Wu, J.-Y. Plasmon-Enhanced Photocurrent in Dye-Sensitized Solar Cells. Sol. *Sol. Energy* **2012**, *86*, 2600–2605.

(36) Qi, J.; Dang, X.; Hammond, P. T.; Belcher, A. M. Highly Efficient Plasmon-Enhanced Dye-Sensitized Solar Cells through Metal@Oxide Core–Shell Nanostructure. *ACS Nano* **2011**, *5*, 7108–7116.

(37) Standridge, S. D.; Schatz, G. C.; Hupp, J. T. Distance Dependence of Plasmon-Enhanced Photocurrent in Dye-Sensitized Solar Cells. *J. Am. Chem. Soc.* **2009**, *131*, 8407–9.

(38) Kim, S.-S.; Na, S.-I.; Jo, J.; Kim, D.-Y.; Nah, Y.-C. Plasmon Enhanced Performance of Organic Solar Cells Using Electrodeposited Ag Nanoparticles. *Appl. Phys. Lett.* **2008**, *93*, 073307.

(39) Yoon, W.-J.; Jung, K.-Y.; Liu, J.; Duraisamy, T.; Revur, R.; Teixeira, F. L.; Sengupta, S.; Berger, P. R. Plasmon-Enhanced Optical Absorption and Photocurrent in Organic Bulk Heterojunction Photovoltaic Devices Using Self-Assembled Layer of Silver Nanoparticles. *Sol. Energy Mater. Sol. Cells* **2010**, *94*, 128–132.

(40) Friebe, V. M.; Delgado, J. D.; Swainsbury, D. J.; Gruber, J. M.; Chanaewa, A.; van Grondelle, R.; von Hauff, E.; Millo, D.; Jones, M. R.; Frese, R. N. Plasmon-Enhanced Photocurrent of Photosynthetic Pigment Proteins on Nanoporous Silver. *Adv. Funct. Mater.* **2016**, *26*, 285–292.

(41) Yen, C.-W.; Chu, L.-K.; El-Sayed, M. A. Plasmonic Field Enhancement of the Bacteriorhodopsin Photocurrent During its Proton Pump Photocycle. *J. Am. Chem. Soc.* **2010**, *132*, 7250–7251.

(42) Nieder, J. B.; Bittl, R.; Brecht, M. Fluorescence Studies into the Effect of Plasmonic Interactions on Protein Function. *Angew. Chem., Int. Ed.* **2010**, *49*, 10217–10220.

(43) Czechowski, N.; Lokstein, H.; Kowalska, D.; Ashraf, K.; Cogdell, R.; Mackowski, S. Large Plasmonic Fluorescence Enhancement of Cyanobacterial Photosystem I Coupled to Silver Island Films. *Appl. Phys. Lett.* **2014**, *105*, 043701.

(44) Hussels, M.; Nieder, J.; Elsässer, C.; Brecht, M. Interactions of Photosystem I with Plasmonic Nanostructures. *Acta Phys. Pol., A* **2012**, *122*, 269.

(45) Kim, I.; Bender, S. L.; Hranisavljevic, J.; Utschig, L. M.; Huang, L.; Wiederrecht, G. P.; Tiede, D. M. Metal Nanoparticle Plasmon-Enhanced Light-Harvesting in a Photosystem I Thin Film. *Nano Lett.* **2011**, *11*, 3091–3098.

(46) Brecht, M.; Hussels, M.; Nieder, J. B.; Fang, H.; Elsässer, C. Plasmonic Interactions of Photosystem I with Fischer Patterns made of Gold and Silver. *Chem. Phys.* **2012**, *406*, 15–20.

(47) Ashraf, I.; Konrad, A.; Lokstein, H.; Skandary, S.; Metzger, M.; Djouda, J. M.; Maurer, T.; Adam, P. M.; Meixner, A. J.; Brecht, M. Temperature Dependence of Metal-Enhanced Fluorescence of Photosystem I from Thermosynechococcus Elongatus. *Nanoscale* **2017**, *9*, 4196–4204.

(48) Govorov, A. O.; Carmeli, I. Hybrid Structures Composed of Photosynthetic System and Metal Nanoparticles: Plasmon Enhancement Effect. *Nano Lett.* **2007**, *7*, 620–625.

(49) Terasaki, N.; Yamamoto, N.; Hiraga, T.; Sato, I.; Inoue, Y.; Yamada, S. Fabrication of Novel Photosystem I–Gold Nanoparticle Hybrids and their Photocurrent Enhancement. *Thin Solid Films* **2006**, *499*, 153–156.

(50) Haynes, C. L.; Van Duyne, R. P. Nanosphere Lithography: a Versatile Nanofabrication Tool for Studies of Size-Dependent Nanoparticle Optics. *J. Phys. Chem. B* **2001**, *105*, 5599–5611.

(51) Mukherjee, D.; May, M.; Khomami, B. Detergent–Protein Interactions in Aqueous Buffer Suspensions of Photosystem I (PS I). *J. Colloid Interface Sci.* **2011**, *358*, 477–484.

(52) Alloway, D. M.; Graham, A. L.; Yang, X.; Mudalige, A.; Colorado, R., Jr; Wysocki, V. H.; Pemberton, J. E.; Randall Lee, T.; Wysocki, R. J.; Armstrong, N. R. Tuning the Effective Work Function of Gold and Silver Using ω-Functionalized Alkanethiols: Varying Surface Composition Through Dilution and Choice of Terminal Groups. *J. Phys. Chem. C* **2009**, *113*, 20328–20334.

(53) Alloway, D. M.; Hofmann, M.; Smith, D. L.; Gruhn, N. E.; Graham, A. L.; Colorado, R.; Wysocki, V. H.; Lee, T. R.; Lee, P. A.; Armstrong, N. R. Interface Dipoles Arising from Self-Assembled Monolayers on Gold: UV-Photoemission Studies of Alkanethiols and Partially Fluorinated Alkanethiols. *J. Phys. Chem. B* **2003**, *107*, 11690–11699.

(54) Khan, M. Z. H. Effect of ITO Surface Properties on SAM Modification: A Review Toward Biosensor Application. *Cogent Eng.* **2016**, *3*, 1170097.

(55) Hong, J.-P.; Park, A.-Y.; Lee, S.; Kang, J.; Shin, N.; Yoon, D. Y. Tuning of Ag Work Functions by Self-Assembled Monolayers of Aromatic Thiols for an Efficient Hole Injection for Solution Processed Triisopropylsilylethynyl Pentacene Organic Thin Film Transistors. *Appl. Phys. Lett.* **2008**, *92*, 143311.

(56) Rusu, P. C.; Brocks, G. Surface Dipoles and Work Functions of Alkylthiolates and Fluorinated Alkylthiolates on Au (111). *J. Phys. Chem. B* **2006**, *110*, 22628–22634.

(57) Cornil, D.; Cornil, J. Work-Function Modification of the (111) Gold Surface Upon Deposition of Self-Assembled Monolayers Based on Alkanethiol Derivatives. *J. Electron Spectrosc. Relat. Phenom.* **2013**, *189*, 32–38.

(58) Feilchenfeld, H.; Chumanov, G.; Cotton, T. M. Photoreduction of Methylviologen Adsorbed on Silver. *J. Phys. Chem.* **1996**, *100*, 4937–4943.

(59) Le, R. K.; Raeeszadeh-Sarmazdeh, M.; Boder, E. T.; Frymier, P. D. Sortase-Mediated Ligation of PsaE-Modified Photosystem I from Synechocystis sp PCC 6803 to a Conductive Surface for Enhanced Photocurrent Production on a Gold Electrode. *Langmuir* **2015**, *31*, 1180−1188.